MRS Communications (2018), *8*, 1470–1476
© Materials Research Society, 2018
doi:10.1557/mrc.2018.220

MRS Communications

Research Letter

Optimizing thermal conduction in bulk polycrystalline $SrTiO_{3-\delta}$ ceramics via oxygen non-stoichiometry

Arash Mehdizadeh Dehkordi, Department of Materials Science and Engineering, Clemson University, Clemson, SC 29634, USA
Sriparna Bhattacharya, Department of Physics and Astronomy, Clemson Nanomaterials Institute, Clemson University, Clemson, SC 29634, USA
Taghi Darroudi, Electron Microscope Facility, Clemson Research Park, Clemson University, Clemson, SC 29634, USA
Mehmet Karakaya, Department of Physics and Astronomy, Clemson Nanomaterials Institute, Clemson University, Clemson, SC 29634, USA
Courtney Kucera, and **John Ballato,** Department of Materials Science and Engineering, Clemson University, Clemson, SC 29634, USA; Center for Optical Materials Science and Engineering Technologies (COMSET), Clemson University, Clemson, SC 29634, USA
Rasheed Adebisi, and **Joseph R. Gladden,** Department of Physics and National Center for Physical Acoustics, University of Mississippi, Oxford, MS 38677, USA
Ramakrishna Podila, and **Apparao M. Rao,** Department of Physics and Astronomy, Clemson Nanomaterials Institute, Clemson University, Clemson, SC 29634, USA; Center for Optical Materials Science and Engineering Technologies (COMSET), Clemson University, Clemson, SC 29634, USA
Husam N. Alshareef, Materials Science and Engineering, King Abdullah University of Science and Technology (KAUST), Thuwal 23955-6900, Saudi Arabia
Terry M. Tritt, Department of Materials Science and Engineering, Clemson University, Clemson, SC 29634, USA; Department of Physics and Astronomy, Clemson University, Clemson, SC 29634, USA

Address all correspondence to Sriparna Bhattacharya at **bbhatta@g.clemson.edu**

(Received 15 August 2018; accepted 30 October 2018)

Abstract

While $SrTiO_3$ exhibits promising electronic transport properties, its high thermal conductivity (κ) is detrimental for its use as a thermoelectric material. Here, we investigate the influence of oxygen non-stoichiometry on κ in bulk $SrTiO_3$ ceramics. A significant reduction in κ was achieved in oxygen deficient $SrTiO_{3-\delta}$, owing to the presence of oxygen vacancies that act as phonon scattering centers. Upon oxidation of $SrTiO_{3-\delta}$, the κ of pristine $SrTiO_3$ was recovered, suggesting that oxygen vacancies were indeed responsible for the reduction in κ. Raman spectroscopy was used as an independent tool to confirm the reduction of oxygen vacancies in $SrTiO_{3-\delta}$ upon oxidation.

Introduction

The first observation of superconductivity in oxides was reported by Schooley et al.[1] in oxygen-deficient (i.e., reduced) semiconducting $SrTiO_{3-\delta}$. Since then, it is well known that deliberate deviation from stoichiometric compositions in many materials can lead to intriguing physical properties. In this regard, oxides have an additional advantage since their stoichiometry can also be tailored during synthesis, for example, by tuning their oxygen stoichiometry. Among oxides, $SrTiO_3$ is regarded as the workhorse of oxide electronics and optoelectronics, which are most sensitive to oxygen stoichiometry, and have been the subject of theoretical[2] and experimental investigations for the past 50 years. Room temperature photoluminescence,[3] bistable electrical switching,[4,5] and optically induced magnetization[6] are few examples of physical properties that have resulted from oxygen non-stoichiometry in $SrTiO_{3-\delta}$. However, the influence of oxygen non-stoichiometry on thermal properties has been overlooked in these oxides. To the best of our knowledge, only a handful of reports on the thermal transport properties of pristine bulk $SrTiO_3$ has been reported.[7–10] Recently, several groups have investigated the thermal conductivity of $SrTiO_3$ thin films as a function of deposition parameters and temperature ($100 < T < 300$ K).[11–13] Understanding the thermal transport and realizing the means to tune thermal conductivity could significantly improve the thermoelectric (TE) performance of $SrTiO_3$, which is attractive for high-temperature TE applications. The potential of any material for TE applications is gauged by its figure-of-merit, ZT, which is inversely proportional to the total thermal conductivity, κ, and directly proportional to the power factor ($\alpha^2\sigma T$) where, σ is the electrical conductivity, α is the Seebeck coefficient, and T the absolute temperature. ZT, in essence, is a measure of the competition between electronic transport (i.e., power factor) and thermal transport (i.e., κ) in TE materials. To enhance ZT, several experimental investigations of $SrTiO_3$ have focused on the reduction of κ mainly through lattice distortion, and mass fluctuation scattering mechanisms arising from the single- or double-doping of the Sr^{2+} and/or Ti^{4+} sites.[14–16] Recently we have investigated the role of phonon scattering mechanisms, particularly strain field scattering and mass fluctuation scattering, on the thermal transport in polycrystalline Y-and Yb-doped $SrTiO_3$ ceramics using a

* A previous error in this article has been corrected, please see doi: 10.1557/mrc.2018.227.

https://doi.org/10.1557/mrc.2018.220 Published online by Cambridge University Press

modified Callaway's model.[17,18] We found that the elastic strain field scattering is the dominant mechanism compared to mass fluctuation scattering that led to the lowest possible κ (~4 W/m/K at 300 K) in Y-doped $SrTiO_3$.[17] This study aims to explore whether oxygen non-stoichiometry can lead to additional phonon scattering sites resulting in a lower κ. In addition, it is well known that in polycrystalline materials, grain boundaries strongly impact the electronic and thermal transport properties. For example, spark-plasma sintering (SPS) of powdered TE materials led to robust bulk materials with enhanced TE properties through the formation of interfaces or grain boundaries. Previously, we reported simultaneous enhancement of electronic transport and a reduction of κ in: (i) Pr-doped $SrTiO_3$ where a substantial enhancement of carrier mobility and ZT originated from SPS generated Pr-rich grain-boundaries,[19,20] (ii) n-type Bi_2Te_3 using a novel chemical-exfoliation SPS (CE-SPS) process that led to charged grain boundaries, which increased σ despite the presence of numerous grain boundaries,[21,22] and (iii) SPS-processed pristine PbTe nanocubes that exhibited a high α due to potential barrier scattering at grain boundaries.[23] In this study, we utilized SPS to generate interfaces in pristine and non-stoichiometric $SrTiO_{3-\delta}$, and found that oxygen vacancies reduce κ. Thus, this work provides an alternate approach for tuning the thermal properties and ultimately improving the performance of $SrTiO_3$-based TEs.

Experimental

Powdered $SrTiO_3$ was prepared using a solid-state reaction wherein stoichiometric amounts of $SrCO_3$ powder (99.9%; Aldrich) and TiO_2 nanopowder (99.5%; Aldrich) were mixed, cold pressed into pellets and calcined in air at ~1300–1400 °C with intermediate grinding and mixing for decarbonation. The calcined pellet was subsequently pulverized into fine powder using a mortar and pestle. About 6 g of resulting powder was then wrapped in graphite foil and loaded into graphite dies. The powder was solidified into a disk (≈12.7 mm diameter and 3 mm thick) using the SPS technique (Dr. Sinter Lab, SPS-515S) under dynamic vacuum at 1400–1500 °C for 5 min (holding time) with DC pulsed current ON/OFF ratio of 12:1. Samples densified using SPS at a high heating rate ~400 °C/min are henceforth referred to as STO-SPS. Unlike synthesis procedures reported in the literature where forming gas (5% H_2 in Ar) was used to reduce the calcined powder, we took advantage of the highly reducing atmosphere in the SPS chamber to tune the oxygen stoichiometry. Both sides of the STO-SPS pellets were polished down by 0.25–0.5 mm to ensure complete removal of the residual carbon from the graphite foil. Density (ρ) of the STO-SPS samples were determined by the Archimedes' method and were found to be >95% of their theoretical values. In order to systematically investigate the effect of non-stoichiometry on the thermal properties, STO-SPS samples were oxidized in air for 70 h at 900 °C. These oxidized samples are hereafter referred to as STO-oxidized. As shown in the inset figures of Fig. 1(b) the STO-SPS sample is opaque and dark gray in color, whereas the STO-oxidized is translucent and orange in color. In addition, (100)-oriented transparent single crystal substrates (hereafter referred to as STO-SC) were purchased (MTI Corp., USA) to serve as a reference. The STO-SC was transparent and with an orange hue, similar to the STO-oxidized. The structure of the calcined powders before SPS, and the STO-SPS and STO-oxidized were characterized using a Rigaku Ultima IV high resolution x-ray diffraction (XRD) with Cu K_α radiation, a Hitachi SU-6600 field emission scanning

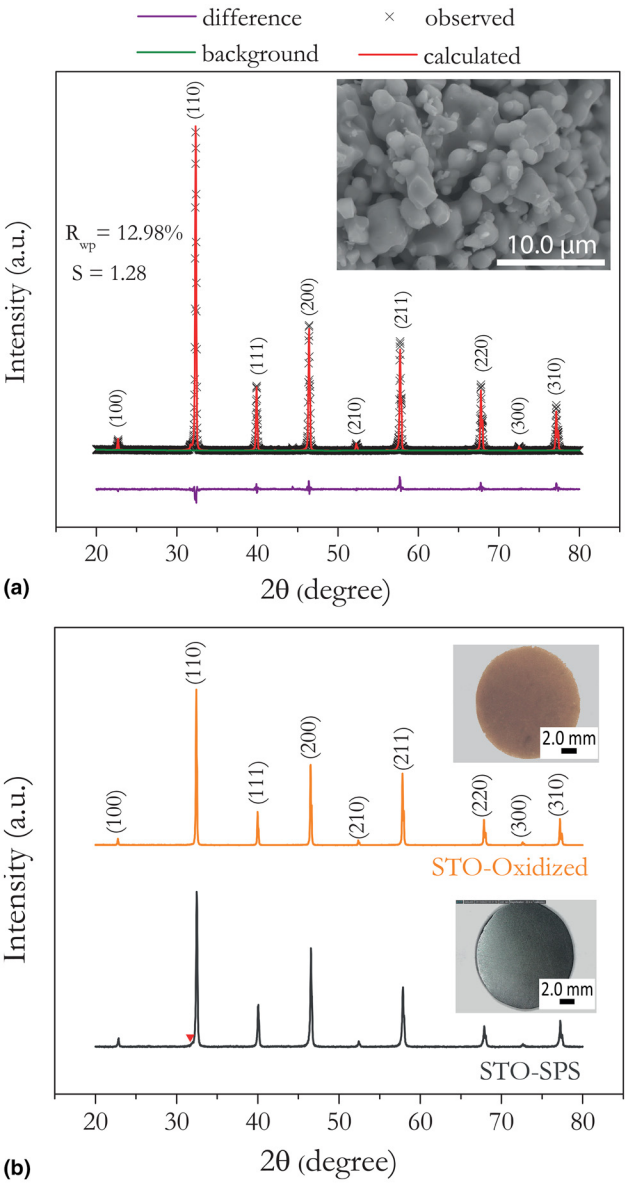


Figure 1. XRD profiles of (a) the as-prepared $SrTiO_3$ powder, before SPS and (b) STO-SPS and STO-oxidized bulk ceramics after SPS indexed to cubic (space group $Pm\bar{3}m$) and pseudo-cubic tetragonal (space group $P4/mmm$), respectively. The inset figure shows: (a) the SEM micrograph of the calcined powder and (b) the opaque and dark gray color of the STO-SPS sample, and the translucent and orange color of the STO-oxidized. The red down-pointing triangle in panel (b) indicates a shoulder arising from non-equivalent peak positions of the (110) and (101) *hkl* values in the tetragonal phase.

https://doi.org/10.1557/mrc.2018.220 Published online by Cambridge University Press

electron microscope (FESEM). Energy dispersive x-ray spectroscopy (EDS, Oxford Instruments) and electron back-scattered diffraction (EBSD) were also performed to investigate the chemical composition and structure. The analysis of the crystal structure and the corresponding x-ray diffraction were performed using the VESTA,[24] PowderCell,[25] DICVOL[26] software packages. Rietveld refinement analysis was performed using the collected XRD patterns with the PDXL software package (Rigaku, Version 1.8.1.0). The quantitative phase analysis to estimate the molar fraction of the secondary phase was also performed using the PDXL software package. The goodness of fit obtained for all the compositions range from $S \sim 1.3$ to 2.0 with R_{wp} values ranging from ~13% to 15% (Fig. 1).

Thermal conductivity was measured over a broad temperature range from 30 to 800 K using two different measurement systems. Above room temperature (300–773 K), thermal conductivity, $\kappa = \rho C_p D$, was calculated from the measured thermal diffusivity, D, specific heat, C_p, and density, ρ using Archimedes' principle. Thermal diffusivity, D, was measured on the pellets using a Netzsch LFA 457 MicroFlash system (300–773 K). To prevent the laser beam from penetrating into the sample and overestimating D, the STO-SC and STO-oxidized were sputter-coated on both sides with a ~0.2 μm thick gold film. The specific heat, C_p was measured on $4 \times 4 \times 1.5$ mm^3 samples cut from the pellets using a Netzsch differential scanning calorimeter (DSC) 404C Pegasus system.

Below room temperature (30–300 K), κ was measured on rectangular bars ($10 \times 2 \times 2$ mm^3) cut from the pellets on a custom-designed measurement system using a steady state technique.[27] κ is corrected for radiation losses above 200 K using the Stefan–Boltzmann law.[27] The uncertainty in measured κ is ±(5–7)% arising from the uncertainty in sample dimensions as well as conductive and convective losses. High- and low-temperature measurements of electrical conductivity and Seebeck coefficient were performed on the same rectangular samples. Carrier concentration of the STO-SPS sample was determined with a Quantum Design Hall system using five-probe configuration under low (5000 Oe) and high (3 T) magnetic fields (30–300 K). Both STO-oxidized and the STO-SC samples were insulating in nature and their carrier concentrations could not be measured.

The velocity of sound (v_s) was estimated from the measured elastic moduli using resonant ultrasound spectroscopy (RUS) from 300 to 800 K.[28] Thermogravimetric analysis (TGA) was also performed to estimate the oxygen content of the samples using a TA Hi-Res TGA 2950 thermogravimetric analyzer in flowing air at 300–1273 K with a constant heating rate of 2 K/min. Lastly, Raman spectra were obtained using a Dilor XY triple grating monochromator equipped with a liquid-nitrogen-cooled CCD detector and a 514.5 nm excitation from an Ar-ion laser coupled with an Olympus 50× microscope.

Results and discussion

Structure and composition

Figure 1(a) shows the XRD pattern of calcined $SrTiO_3$ powder. The main reflections in the pattern can be readily indexed to the $SrTiO_3$ cubic perovskite lattice (space group $Pm\bar{3}m$) with a lattice parameter $a = 3.906$ Å. Phase analysis shows the presence of 1–2 mol% secondary phase at the interface of the $SrCO_3$ and TiO_2 powders, formed during the solid state reaction. The inset shows the SEM micrograph of the calcined powder with an average particle size of ~3–5 μm, which was then densified by SPS to form the STO-SPS sample. As shown in Fig. 1(a), low values of the least square refinement parameter for the whole pattern ($R_{wp} \sim 13\%$) and goodness of fit ($S \sim 1.3$) were obtained. Figure 1(b) shows the diffraction patterns of the STO-SPS and STO-oxidized. The diffraction pattern of the STO-SPS pellet is indexed to pseudo-cubic tetragonal (space group $P4/mmm$) lattices with lattice parameters, $a = b =$ 3.9177 Å, and $c = 3.887$ Å.[29] Upon oxidizing in air to form STO-oxidized pellet, the diffraction pattern reverts to that expected for $SrTiO_3$ cubic perovskite lattice (space group $Pm\bar{3}m$, lattice parameter $a = 3.906$ Å) in which oxygen vacancies are absent. The crystal structure of STO-SPS and STO-oxidized were further verified using EBSD and the analysis of the unique "kikuchi bands" revealed that the average electron-diffraction pattern of the grains can be indexed to pseudo-cubic tetragonal [Fig. 2(a)] and cubic lattices [Fig. 2(b)] in the STO-SPS and STO-oxidized respectively, consistent with the x-ray diffraction analysis. In general, EBSD results cannot conclusively differentiate between two crystal structures unless there is significant difference between unit cell dimensions. Nonetheless, the SEM micrographs suggest that both samples possess similar average grain size of ~50–100 μm (Fig. 2), which is due to grain growth that occurred during SPS. It should be noted that oxidation did not affect the average grain size.

Oxygen non-stoichiometry and thermal transport

The oxygen uptake by each sample was estimated from their weight change using TGA (Fig. 3) using STO-SC as a reference. As expected, STO-oxidized exhibited similar weight change as the STO-SC, however the STO-SPS sample gained 0.5% in weight due to the uptake of oxygen which corresponds to an oxygen deficiency per formula unit (δ) of 0.06 (i.e., $SrTiO_{2.94}$ assuming a stoichiometric cation ratio).

Figure 4(a) shows the total κ of STO-SPS and STO-oxidized samples relative to that of STO-SC. To the best of our knowledge, this is the first report of κ for $SrTiO_3$ (either poly- or single-crystalline) over a broad temperature range of 30–800 K. The low-temperature κ of STO-SC is in agreement with the reported κ in the range 50–225 K by Steigmeier[9] and Suemune[8], above which it deviated due to radiation losses. A significant reduction in κ, 50% at 100 K and 40% at 300 K, was observed for the STO-SPS sample in comparison with that of STO-SC. Upon oxidation, κ increased by 30% at 300 K toward the corresponding value for STO-SC. Henceforth, we focus our discussion on the properties of STO-SPS since it exhibited the lowest κ [Fig. 4(a)]. To

https://doi.org/10.1557/mrc.2018.220 Published online by Cambridge University Press

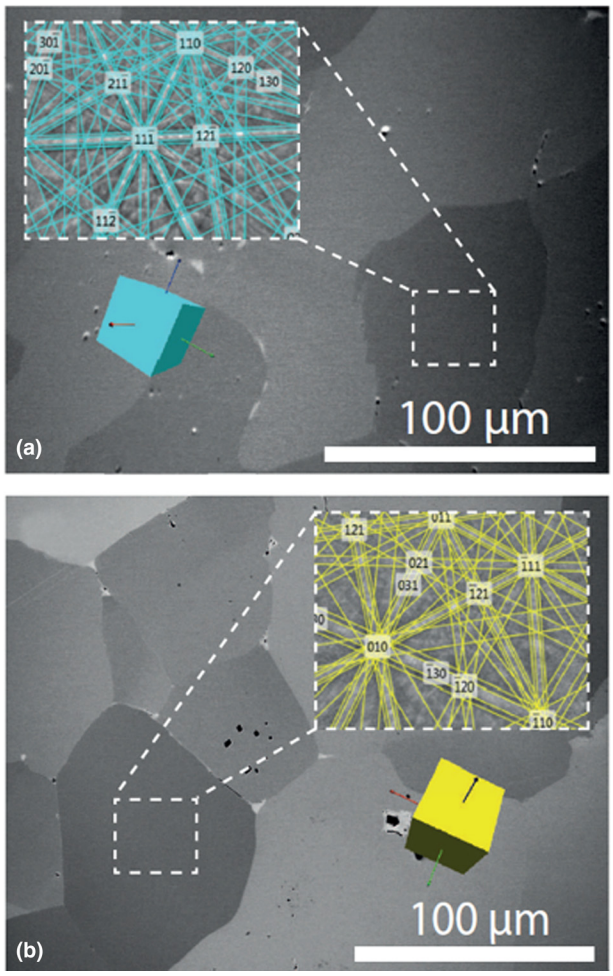


Figure 2. EBSD analysis of (a) the STO-SPS and (b) STO-oxidized bulk ceramics. The inset figures exhibit the unique kikuchi patterns of the (a) the pseudo-cubic tetragonal (space group *P4/mmm*) and (b) and cubic (space group $Pm\bar{3}m$) lattices. Similar grain sizes are observed in both the STO-SPS and STO-oxidized bulk ceramics.

understand the underlying mechanism for reduction in κ for STO-SPS sample the phonon mean free path was estimated as a function of temperature [Fig. 4(b)]. From kinetic theory, the average phonon mean free path (l_{ph}) is related to κ_L as $\kappa_L = (1/3)C_p v_s l_{ph}$, where κ_L is the lattice thermal conductivity, C_p the specific heat, and v_s the phonon velocity. The high-temperature C_p is measured for both samples and is within 10% of each other over the whole temperature range. κ_L in STO-SPS sample was determined from the Wiedemann–Franz relationship, $\kappa_L = \kappa - \sigma LT$, where, $\kappa_E = \sigma LT$ is the electronic contribution to κ and L the Lorenz number for a degenerate semiconductor ($L = 2.0 \times 10^{-8}\ V^2/K^2$).[30] Owing to the insulating nature of the STO-SC samples in the temperature range studied, it is evident that $\kappa \approx \kappa_L$. For the STO-SPS sample, v_s (~5172 at 300 K) was estimated from its measured elastic moduli using RUS and density,[17] which is close to the reported value of v_s for the STO-SC sample at this

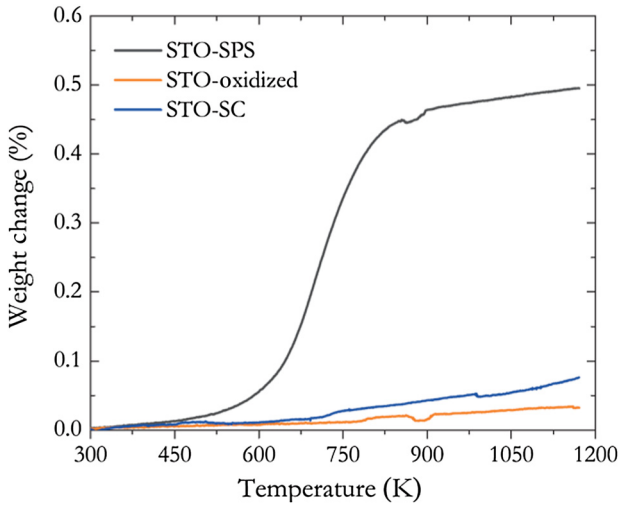


Figure 3. Weight change as a function of temperature for polycrystalline STO-SPS and STO-oxidized samples and single-crystalline STO-SC substrate heated in air with 2 K/min heating rate.

temperature.[31] This suggests that the reduction in l_{ph} does not originate from a reduction in either C_p or v_s but from an inherently different κ_L. As expected, both STO-oxidized and STO-SPS samples exhibit a lower κ ($\approx\kappa_L$) [Fig. 4(a)] than that of the STO-SC sample due to the presence of grain boundaries. However, the STO-SPS sample exhibits a further reduction of κ due to phonon scattering by oxygen vacancies.

In the Debye model using relaxation time approximation the Callaway's phenomenological model for κ_L is given by[32]:

$$\kappa_L(x) = \frac{k_B}{2\pi^2 v_s}\left(\frac{k_B T}{\hbar}\right)^3 \int_0^{\Theta_D/T} \frac{x^4 e^x}{\tau_{ph}^{-1}(e^x - 1)^2} dx \qquad (1)$$

where $x = \hbar\omega/k_B T$ is the reduced phonon frequency, ω the phonon frequency, $\hbar$ the reduced Planck's constant, k_B the Boltzmann constant, and T the absolute temperature. The total relaxation time (τ_{ph}) is given by the Matthiessen's rule, $\tau_{ph}^{-1} = \tau_{PD}^{-1} + \tau_U^{-1} + \tau_B^{-1}$, consisting of phonon scattering by point defects (τ_{PD}), the anharmonic phonon–phonon or Umklapp scattering (τ_U), and the phonon-boundary scattering (τ_B), respectively. The relaxation time for point defect scattering estimated by Klemens[33] is given by $\tau_{PD}^{-1} = A\omega^4 = (V/4\pi v_s^3)\omega^4\Gamma$ which represents a combination of impurity and isotope scattering where $\Gamma = \sum_i x_i[(\Delta M_i/M)^2]$ is the mass fluctuation scattering parameter and V is the volume per atom. As proposed by Klemens,[34] oxygen vacancies act as point defect scattering centers for phonons, and the effective mass of vacancies is given by $\Delta M/M = -(M_a/M) - 2$, where M is the average mass per atom, M_a is the mass of the missing atom, and the term -2 accounts for the potential energy of the missing atom. Assuming there are no additional defects present in the STO-oxidized sample, the $\Delta M/M$ term arising from oxygen vacancies dominates the point defect scattering

https://doi.org/10.1557/mrc.2018.220 Published online by Cambridge University Press

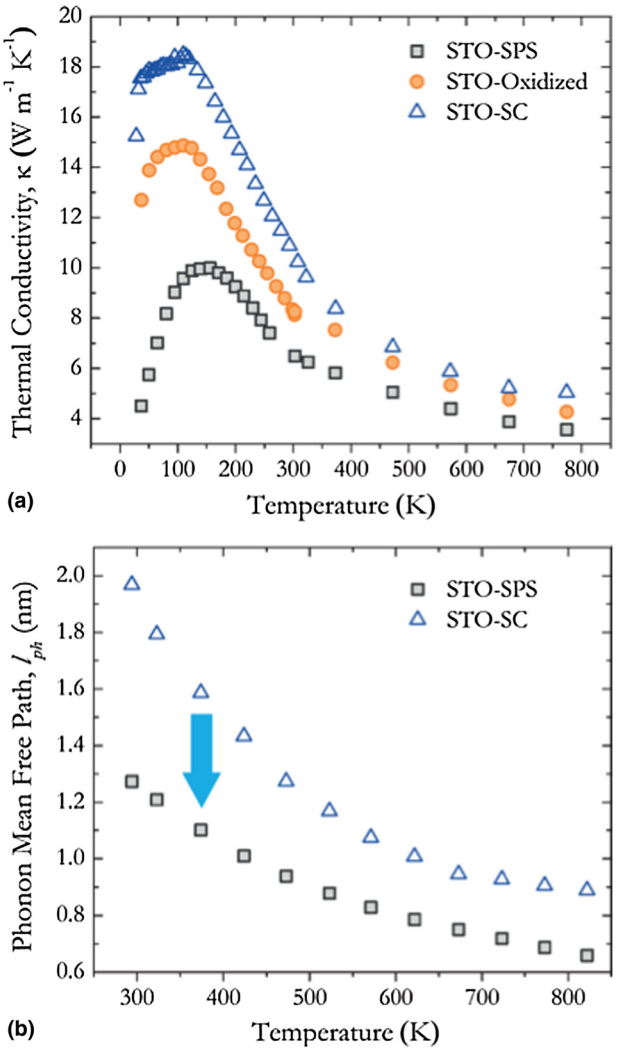


Figure 4. (a) Total thermal conductivity of STO-SPS, STO-oxidized, and STO-SC samples. (b) Phonon mean free path estimated from measured and reported mean velocity of sound for STO-SPS and STO-SC samples.

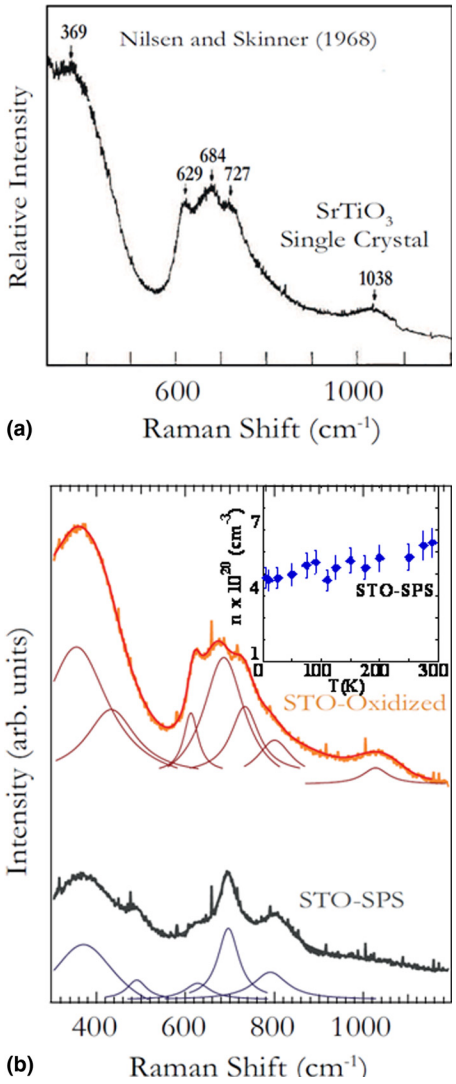


Figure 5. Raman spectra of (a) pristine $SrTiO_3$ single crystal at 300 K using a 488 nm laser line, reported by Nilsen and Skinner (reproduced from Ref. 35, with permission from AIP Publishing). (b) STO-SPS and STO-oxidized samples using a 514.5 nm Ar-ion laser excitation at 300 K. The inset in (b) shows the carrier concentration (n) of STO-SPS sample as a function of temperature from 10 to 300 K.

term in the STO-SPS sample. Thus, it may be concluded that mass fluctuation scattering due to oxygen vacancies is a dominant phonon scattering mechanism in the STO-SPS sample leading to the significant reduction in κ [Fig. 4(a)].

Raman spectroscopy

In order to further confirm the presence of oxygen vacancies, we compared the room temperature Raman spectra of STO-SPS and STO-oxidized samples with that of the standard STO-SC[35] (Fig. 5). Previously, Tenne et al.[36] observed the emergence of otherwise forbidden first order Raman peaks in reduced and re-oxidized $SrTiO_3$ single crystals. In other words, a peak at 700/cm emerges when the STO is reduced, and the measured carrier concentration reported by Tenne et al. was on the order of 10^{19}/cm^3. Inferring from the conclusions drawn by Tenne et al. in their combined Raman and electrical transport study,[36] the Raman peak at ~700/cm in STO-SPS suggests a carrier concentration $n > 10^{19}$/cm^3 arising from oxygen vacancies. This value of n is also consistent with the value measured in our electrical transport properties of the STO-SPS sample [inset in Fig. 5(b)]. Not surprisingly, the Raman peak at ~700/cm disappears in the STO-oxidized due to a reduction in oxygen vacancies. Indeed, the Raman spectrum of STO-oxidized showed four peaks (three peaks between 600 and 750/cm and one peak at 1040/cm that are expected for the stoichiometric $SrTiO_3$) distinct from the Raman peaks in the STO-SPS sample. These new second order features (~600–750/cm) in the Raman spectrum of STO-oxidized showed an excellent match to the Raman peaks of $SrTiO_3$ single crystals

https://doi.org/10.1557/mrc.2018.220 Published online by Cambridge University Press

studied by Nilsen and Skinner.[35] These three peaks at 629, 684, and 727/cm in single crystalline $SrTiO_3$ were attributed to combination or overtones of transverse modes, and the band at 1038/cm to a superposition of longitudinal and transverse optical phonon overtones. Juxtaposing the disappearance of 700/cm peak and the appearance of four new peaks in the STO-oxidized samples, we conclude that the oxygen vacancies are significantly reduced upon oxidation.

Conclusions

In summary, we studied the role of oxygen non-stoichiometry on κ, and report a significant reduction in κ in the spark-plasma sintered $SrTiO_{2.94}$ (STO-SPS) compared with its pristine single crystalline counterpart $SrTiO_3$ (STO-SC). Upon oxidation of the STO-SPS sample, a higher κ (~25% at 300 K) is measured in the STO-oxidized compared with that of the STO-SPS sample. This confirms the role of oxygen vacancies that act as dominant phonon scattering centers in the STO-SPS sample. Interestingly, the STO-SPS sample also exhibits a carrier concentration $n \sim 10^{20}/cm^3$, in contrast to the electrically insulating behavior observed in both STO-oxidized and STO-SC samples. The presence of oxygen non-stoichiometry in STO-SPS sample is independently confirmed by thermogravimetric measurements and Raman spectroscopy.

Acknowledgments

The research was supported by KAUST-Clemson Faculty Initiated collaboration grant. The authors would like to thank W.G. Nilsen and J.G. Skinner[35] for the reprint their Raman spectra to directly compare with our Raman spectra. The authors would like to acknowledge useful discussions with Dr. Colin McMillen (Clemson University) on the XRD analysis of these samples and Mr. Herbert Behlow on stoichiometric analysis.

References

1. J.F. Schooley, W.R. Hosler, and M.L. Cohen: Superconductivity in semiconducting $SrTiO_3$. *Phys. Rev. Lett.* **12**, 474 (1964).
2. C. Mitra, C. Lin, J. Robertson, and A.A. Demkov: Electronic structure of oxygen vacancies in $SrTiO_3$ and $LaAlO_3$. *Phys. Rev. B* **86**, 155105 (2012).
3. D. Kan, T. Terashima, R. Kanda, A. Masuno, K. Tanaka, S. Chu, H. Kan, A. Ishizumi, Y. Kanemitsu, Y. Shimakawa, and M. Takano: Blue-light emission at room temperature from Ar^+-irradiated $SrTiO_3$. *Nat. Mater.* **4**, 816 (2005).
4. K. Szot, W. Speier, G. Bihlmayer, and R. Waser: Switching the electrical resistance of individual dislocations in single-crystalline $SrTiO_3$. *Nat. Mater.* **5**, 312 (2006).
5. M. Janousch, G.I. Meijer, U. Staub, B. Delley, S.E. Karg, and B. P. Andreasson: Role of oxygen vacancies in Cr-doped $SrTiO_3$ for resistance-change memory. *Adv. Mater.* **19**, 2232 (2007).
6. W.D. Rice, P. Ambwani, J.D. Thompson, C. Leighton, and S.A. Crooker: Revealing optically induced magnetization in $SrTiO_3$ using optically coupled SQUID magnetometry and magnetic circular dichroism. *J. Vac. Sci. Technol. B, Nanotechnol. Microelectron. Mater. Process. Meas. Phenom.* **32**, 04E102 (2014).
7. I. Yoshida: Thermal conduction in ferroelectric ceramics. *J. Phys. Soc. Jpn.* **15**, 2211 (1960).
8. Y. Suemune: Thermal conductivity of $BaTiO_3$ and $SrTiO_3$ from 4.5 to 300 K. *J. Phys. Soc. Jpn.* **20**, 174 (1965).
9. E.F. Steigmeier: Field effect on the Cochran modes in $SrTiO_3$ and $KTaO_3$. *Phys. Rev.* **168**, 523 (1968).
10. Y. Wang, K. Fujinami, R. Zhang, C. Wan, N. Wang, Y. Ba, and K. Koumoto: Interfacial thermal resistance and thermal conductivity in nanograined $SrTiO_3$. *Appl. Phys. Express* **3**, 031101 (2010).
11. E. Breckenfeld, R. Wilson, J. Karthik, A.R. Damodaran, D.G. Cahill, and L. W. Martin: Effect of growth induced (non)stoichiometry on the structure, dielectric response, and thermal conductivity of $SrTiO_3$ thin films. *Chem. Mater.* **24**, 331 (2012).
12. B.M. Foley, H.J. Brown-Shaklee, J.C. Duda, R. Cheaito, B.J. Gibbons, D. Medlin, J.F. Ihlefeld, and P.E. Hopkins: Thermal conductivity of nanograined $SrTiO_3$ thin films. *Appl. Phys. Lett.* **101**, 231908 (2012).
13. D.-W. Oh, J. Ravichandran, C.-W. Liang, W. Siemons, B. Jalan, C. M. Brooks, M. Huijben, D.G. Schlom, S. Stemmer, L.W. Martin, A. Majumdar, R. Ramesh, and D.G. Cahill: Thermal conductivity as a metric for the crystalline quality of $SrTiO_3$ epitaxial layers. *Appl. Phys. Lett.* **98**, 221904 (2011).
14. S.R. Popuri, A.J.M. Scott, R.A. Downie, M.A. Hall, E. Suard, R. Decourt, M. Pollet, and J.W.G. Bos: Glass-like thermal conductivity in $SrTiO_3$ thermoelectrics induced by A-site vacancies. *RSC Adv.* **4**, 33720 (2014).
15. B. Zhang, J. Wang, T. Zou, S. Zhang, X. Yaer, N. Ding, C. Liu, L. Miao, Y. Li, and Y. Wu: High thermoelectric performance of Nb-doped $SrTiO_3$ bulk materials with different doping levels. *J. Mater. Chem. C* **3**, 11406 (2015).
16. D. Srivastava, C. Norman, F. Azough, M.C. Schäfer, E. Guilmeau, and R. Freer: Improving the thermoelectric properties of $SrTiO_3$-based ceramics with metallic inclusions. *J. Alloys Compd.* **731**, 723 (2018).
17. S. Bhattacharya, A. Mehdizadeh Dehkordi, S. Tennakoon, R. Adebisi, J. R. Gladden, T. Darroudi, H.N. Alshareef, and T.M. Tritt: Role of phonon scattering by elastic strain field in thermoelectric $Sr_{1-x}Y_xTiO_{3-\delta}$. *J. Appl. Phys.* **115**, 223712 (2014).
18. S. Bhattacharya, A.M. Dehkordi, H.N. Alshareef, and T.M. Tritt: Synthesis-property relationship in thermoelectric $Sr_{1-x}Yb_xTiO_{3-\delta}$ ceramics. *J. Phys. D: Appl. Phys.* **47**, 385302 (2014).
19. A. Mehdizadeh Dehkordi, S. Bhattacharya, T. Darroudi, J.W. Graff, U. Schwingenschlögl, H.N. Alshareef, and T.M. Tritt: Large thermoelectric power factor in Pr-doped $SrTiO_{3-\delta}$ ceramics via grain-boundary-induced mobility enhancement. *Chem. Mater.* **26**, 2478 (2014).
20. A.M. Dehkordi, S. Bhattacharya, J. He, H.N. Alshareef, and T.M. Tritt: Significant enhancement in thermoelectric properties of polycrystalline Pr-doped $SrTiO_{3-\delta}$ ceramics originating from nonuniform distribution of Pr dopants. *Appl. Phys. Lett.* **104**, 3 (2014).
21. P. Puneet, R. Podila, M. Karakaya, S. Zhu, J. He, T.M. Tritt, M. S. Dresselhaus, and A.M. Rao: Preferential scattering by interfacial charged defects for enhanced thermoelectric performance in few-layered n-type Bi_2Te_3. *Sci. Rep.* **3**, 1 (2013).
22. F. Liu, L. Hu, M. Karakaya, P. Puneet, R. Rao, R. Podila, S. Bhattacharya, and A.M. Rao: A micro-Raman study of exfoliated few-layered n-type $Bi_2Te_{2.7}Se_{0.3}$. *Sci. Rep.* **7**, 16535 (2017).
23. B. Khasimsaheb, S. Neeleshwar, M. Srikanth, S. Bathula, B. Gahtori, A. K. Srivsatava, A. Dhar, A. Sankarakumar, B.K. Panigrahi, S. Bhattacharya, R. Polida, and A.M. Rao: Thermoelectric properties of spark plasma sintered lead telluride nanocubes. *J. Mater. Res.* **30**, 1 (2015).
24. K. Momma and F. Izumi: VESTA 3 for three-dimensional visualization of crystal, volumetric and morphology data. *J. Appl. Crystallogr.* **44**, 1272 (2011).
25. W. Kraus and G. Nolze: POWDER CELL – A program for the representation and manipulation of crystal structures and calculation of the resulting x-ray powder patterns. *J. Appl. Crystallogr.* **29**, 301 (1996).
26. A. Boultif and D. Louër: Powder pattern indexing with the dichotomy method. *J. Appl. Crystallogr.* **37**, 724 (2004).
27. A.L. Pope, B. Zawilski, and T.M. Tritt: Description of removable sample mount apparatus for rapid thermal conductivity measurements. *Cryogenics* (*Guildf*). **41**, 725 (2001).
28. G. Li and J.R. Gladden: High temperature resonant ultrasound spectroscopy: a review. *Int. J. Spectrosc.* **2010**, 1 (2010).
29. W. Gong, H. Yun, Y.B. Ning, J.E. Greedan, W.R. Datars, and C.V. Stager: Oxygen-deficient $SrTiO_{3-x}$, $x = 0.28$, 0.17, and 0.08. crystal growth,

https://doi.org/10.1557/mrc.2018.220 Published online by Cambridge University Press

crystal structure, magnetic, and transport properties. *J. Solid State Chem.* **90**, 320 (1991).
30. T.M. Tritt: Thermoelectric phenomena, materials, and applications. *Annu. Rev. Mater. Res.* **41**, 433 (2011).
31. A. Migliori, J.L. Sarrao, W.M. Visscher, T.M. Bell, M. Lei, Z. Fisk, and R. G. Leisure: Resonant ultrasound spectroscopic techniques for measurement of the elastic moduli of solids. *Phys. B: Condens. Matter* **183**, 1 (1993).
32. J. Callaway: Model for lattice thermal conductivity at low temperatures. *Phys. Rev.* **113**, 1046 (1959).
33. P. Klemens: Thermal resistance due to point defects at high temperatures. *Phys. Rev.* **119**, 507 (1960).
34. P.G. Klemens: Phonon scattering by oxygen vacancies in ceramics. *Phys. B: Condens. Matter* **263–264**, 102 (1999).
35. W.G. Nilsen and J.G. Skinner: Raman spectrum of strontium titanate. *J. Chem. Phys.* **48**, 2240 (1968).
36. D.A. Tenne, I.E. Gonenli, A. Soukiassian, D.G. Schlom, S. M. Nakhmanson, K.M. Rabe, and X.X. Xi: Raman study of oxygen reduced and re-oxidized strontium titanate. *Phys. Rev. B – Condens. Matter Mater. Phys.* **76**, 1 (2007).

https://doi.org/10.1557/mrc.2018.220 Published online by Cambridge University Press